Structural basis for tRNA modification by Elp3 from *Dehalococcoides mccartyi*

Sebastian Glatt[1,2], **Rene Zabel**[#3], **Olga Kolaj-Robin**[#4,5,6], **Osita F. Onuma**[3], **Florence Baudin**[1,7], **Andrea Graziadei**[1], **Valerio Taverniti**[4,5,6], **Ting-Yu Lin**[2], **Frauke Baymann**[8], **Bertrand Seraphin**[4,5,6], **Karin D. Breunig**[3], and **Christoph W. Müller**[1]

[1]European Molecular Biology Laboratory, Structural and Computational Biology Unit, Heidelberg, Germany [2]Max Planck Research Group at the Malopolska Centre of Biotechnology, Jagiellonian University, Krakow, Poland [3]Institute of Biology, Martin-Luther-University Halle-Wittenberg, Halle (Saale), Germany [4]Université de Strasbourg, IGBMC UMR 7104, Illkirch, France [5]CNRS, IGBMC UMR 7104, Illkirch, France [6]Inserm, IGBMC U964, Illkirch, France [7]Unit of Virus Host-Cell Interactions (UMI 3265), University Grenoble Alpes-CNRS-EMBL, Grenoble, France [8]Laboratoire de Bioénergétique et Ingénierie des Protéines, BIP/CNRS, UMR7281, AMU, Marseille, France

[#] These authors contributed equally to this work.

Abstract

During translation elongation decoding is based on the recognition of codons by corresponding tRNA anticodon triplets. Molecular mechanisms that regulate global protein synthesis via specific base modifications in tRNA anticodons have recently received increasing attention. The conserved eukaryotic Elongator complex specifically modifies uridines located in the wobble base position of tRNAs. Here, we present the crystal structure of *Dehalococcoides mccartyi* Elp3 (DmcElp3) at 2.15 Å resolution. Our results reveal the unexpected arrangement of Elp3 lysine acetyl transferase (KAT) and radical S-adenosyl-methionine (SAM) domains that share a large interface to form a composite active site and tRNA binding pocket with an iron sulfur cluster located in the dimerization interface of two DmcElp3 molecules. Structure-guided mutagenesis studies of yeast Elp3 confirm the relevance of our findings for eukaryotic Elp3s and for understanding Elongator's role in the onset of various neurodegenerative diseases and cancer in humans.

Keywords

Elongator; Elp3; tRNA modification; X-ray crystallography; yeast; *Saccharomyces cerevisiae*

Introduction

The speed of ribosomes during the elongation phase of translation is not uniform along mRNAs[1]. In particular, transient pausing events support domain folding, as proteins begin to attain their three dimensional structure in concert with their synthesis[2]. As tRNA selection in the A-site of ribosomes is a rate-limiting step during elongation phase, the use of synonymous codons influences local elongation speed and aids co-translational protein folding[3,4]. Notably, specific base modifications in the wobble base position of tRNAs enhance binding to the A site of the ribosome[5,6]. Hence, it was shown that the speed of translating ribosomes indeed decreases on respective codons due to the lack of certain wobble base modification. Furthermore, these synthesis rate variations lead to altered folding dynamics of nascent polypeptide chains and ultimately result in large amounts of misfolded and aggregated proteins. Therefore, these modifications act as gate keepers that maintain the homeostasis of whole cellular proteomes[7].

Two copies of each of the highly conserved six subunits of the eukaryotic Elongator complex (Elp1–6) constitute a large macromolecular complex, which in combination with additional modification pathways conducts the formation of 5-methoxycarbonylmethyl-uridine (mcm^{5}U), 5-methoxycarbonylmethyl-2-thiouridine (mcm^{5}s^{2}U), and 5-carbamoylmethyluridine (ncm^{5}U) on uridines in the wobble base position of tRNAs[8–11]. All six subunits are equally important for its modification activity[12], required for Elongator complex integrity (except Elp2), and mainly localize to the cytoplasm[13]. Homologs of the six Elongator subunits have been identified in eukaryotes from yeast to human. Hence, the tRNA modification activity of Elongator has been shown to be important for multiple cellular activities in yeast[9], flies[14], worms[15], fish[16], plants[17], mice[18], and humans[19]. The Elongator protein 3 (Elp3) subunit is suspected to harbor the active site of the complex as it was predicted to contain a lysine acetyl transferase (KAT)[20] and a radical S-adenosyl-methionine (SAM) binding domain[21], together capable of conducting suitable chemistry for the initial cm^{5}U formation[10]. Almost all archaea, a small number of bacteria and two viruses also possess Elp3 homologues, but lack genes encoding the other five Elongator subunits, suggesting the ancient nature and conserved function of the enzymatic core subunit of the complex. In humans, specific mutations in Elongator subunits are correlated with the development of certain neurodegenerative diseases[16,22] and cancer[23] stressing the clinical importance of understanding the underlying molecular mechanisms.

High-resolution structural information recently became available for the homo-dimer of the Elp1 C-terminus[23], Elp2[24], the Elp456 heterohexamer[25,26], and the accessory factors Killer toxin insensitive 11 (Kti11) and Kti13[27,28]. Here, we set out to obtain structural and functional insight into the enzymatic core subunit Elp3 of the Elongator complex that carries out the proposed tRNA modification reaction. The detailed mechanism of this reaction has remained unclear[11], because so far no structural information on Elp3 has been available. We

determined the crystal structure of full length Elp3 from *Dehalococcoides mccartyi* (DmcElp3), which reveals the molecular details of the individual KAT and SAM domains and their relative orientation to each other. Our data further support the view that the intensively discussed[29–31] genuine cellular function of the Elongator complex is the regulation of translation elongation, which is involved in the onset of various neurodegenerative diseases, cancer and intellectual disabilities[16,32,33].

Results

Crystal structure of DmcElp3

We cloned and recombinantly expressed full length Elp3 from *D. mccartyi*, an anaerobic dehalogenating bacterium recently isolated from toxic waste[34,35]. DmcElp3 showed very high sequence conservation with Elp3 from other species (e.g. *Saccharomyces cerevisiae* Elp3 41.4% identity and human Elp3 42.2% identity; see Supplementary Note 1). We obtained crystals of purified DmcElp3, solved the structure and refined it to R/R_{free} values of 19.1%/21.9% at 2.15 Å resolution (Table 1 and Supplementary Fig. 1a). The compact structure of DmcElp3 showed a previously unobserved arrangement of KAT and SAM domains, which are connected by a zinc binding motif and share a large domain interface (~1700 $Å^2$) (Fig. 1a). The SAM domain showed the highest structural similarity to bacterial RlmN (Fig. 1b), which is known to bind RNA and employ radical chemistry to catalyze methylation of A_{2503} in the 23S rRNA[36] and A_{37} in certain tRNAs[37,38]. The KAT domain is most similar to members of the Gcn5 family of canonical histone acetyl transferases (HATs)[39] (Fig. 1c). The topology of secondary structure elements of the individual domains (Supplementary Fig. 1b,c) are similar to other SAM and HAT containing proteins, although the KAT domain has an additional seventh β-strand (β13) and is missing the first two helices in the N-terminus (α1 and α2; (Fig. 1c)). Strikingly, the SAM domain fully blocked the canonical substrate or peptide binding site of the KAT domain (Fig. 1c and Supplementary Fig. 1d), which precludes the hypothesis that recombinant Elp3 is able to acetylate lysine residues in histone tails[20] or other protein substrates[40,41].

Characterization of the iron-sulfur cluster in DmcElp3

Size exclusion chromatography indicated two discrete oligomeric states of DmcElp3 purified under aerobic and anaerobic conditions. Strikingly, the dimeric peak showed a strong reddish color, whereas the monomeric fractions remained colorless (Fig. 2a). UV absorbance spectroscopy with a broad signal in the 400 to 600 nm region and electron paramagnetic resonance (EPR) measurements suggested the presence of a [Fe–S] cluster in the dimer (Supplementary Fig. 2a,b), whereas no EPR active species could be detected in the aerobically purified monomer. The optical spectrum exhibited a peak at 410 nm characteristic for [4Fe–4S] clusters and gentle shoulders at 440 and 510 nm suggesting the presence of some additional [2Fe–2S] cluster-containing protein in the sample. The amplitude of the signal at 410 nm ($\varepsilon_{410} = 16$ mM^{-1}cm^{-1})[42] suggested that nearly the full complement of protein contained [Fe–S] clusters, mainly in the [4Fe–4S] form. EPR analyses of the anaerobic and aerobic purified enzyme revealed two distinct classes of signals (Supplementary Fig. 2b). A broad and fast relaxing EPR signal was consistent with a [4Fe–4S] cluster in 3/2 spin state[43,44]. Quantification of this signal indicated that the

corresponding cluster was only present in a minor fraction of the protein. Further signals around g=2, observed at 15 K and 50 K, reflect the presence of a heterogeneous population of [Fe–S] clusters in the spin ½ state in about 1-10 % of the sample. EPR did not allow for a clear-cut attribution of these signals to [2Fe–2S] or [4Fe–4S] clusters.

In the crystals, which were only obtained using the dimer, we observed a [2Fe–2S] cluster located at the interface of two DmcElp3 molecules related by a crystallographic dyad (Fig. 2b). In particular, residues C27 and C30 from two neighboring DmcElp3s are involved in the coordination of one [2Fe–2S] cluster. We confirmed the cluster species in our structure by using a full dataset collected close to the absorption edge of iron (λ=1.7377 Å) to calculate anomalous difference Fourier maps that clearly identified peaks for only two coordinated iron ions (Fig. 2c). In addition, we also used anomalous difference Fourier maps (λ=1.28238 Å) to confirm that residues C310, C312 and C315, which are conserved in archaeal Elp3s but not in eukaryotic Elp3s, specifically coordinate a zinc ion (Fig. 2c).

We assumed that the discrepancy between the prevalence of the [4Fe–4S] cluster in solution and the [2Fe–2S] cluster in the crystal structure resulted from disintegration of the [4Fe–4S] cluster during purification and crystallization under aerobic conditions or from induced radiation damage during the X-ray data collection. Importantly, non-physiological reduction of the cluster by dithionite to obtain the EPR-detectable paramagnetic state may have also contributed to the transformation of the [4Fe–4S] cluster to a [2Fe–2S] cluster explaining the low abundance of the [4Fe–4S] cluster and the presence of [2Fe–2S] cluster during our EPR measurements. Indeed, the [4Fe–4S] cluster in 3/2 spins state observed in our EPR measurements is known to be particularly sensitive and unstable under aerobic conditions[45] and in the case of aerobically purified dimer we observed discoloration of the sample upon reduction with dithionite. In summary, our observations are in agreement with a previous study that also identified the presence of a [4Fe–4S] cluster (also in substoichiometric amounts) in a truncated form of the SAM domain of Elp3 from *Methanocaldococcus jannaschii*[21]. The distinct peak at ~320 nm present in DmcElp3 spectrum that could argue for [2Fe–2S] cluster was also observed in another [4Fe–4S]-containing unusual SAM radical enzyme, Dph2[46].

Dimerization of DmcElp3

Due to its involvement in dimerization, the conformation and localization of the iron-sulfur cluster and its coordination loop were different from any known radical SAM domain. The dimerization interface was additionally stabilized by strong hydrogen networks (Fig. 2b) and involved also conserved residues that were not directly participating in [2Fe–2S] coordination. Mutational analyses showed that I28A and Y29A, but also R136A and R173A mutations, strongly decreased dimer formation (Supplementary Fig. 2c). Interestingly, mutations of residues C27S and C30S, which were both crucial for iron-sulfur cluster coordination, still allowed dimer formation although to a lesser extent. Dimerization clearly increased the thermostability of wild type (wt) and mutated DmcElp3 and none of the generated single point mutations in this study led to misfolded protein (Supplementary Fig. 2d).

Because of the high sequence conservation, we were able to test the role of equivalent residues in ScElp3 on tRNA modification activity *in vivo* by several previously established yeast assays27. In detail, the γ-toxin assay relies on galactose-inducible expression of a tRNA anticodon nuclease that cleaves mcm^5s^2 modified tRNAs resulting in growth inhibition. Growth on galactose medium reported absence of this modification due to Elongator deficiency. The SUP4 assay makes use of strains carrying the *SUP4* nonsense suppressor tRNA gene. Suppression of ochre stop codons by *SUP4* tRNA also depends on Elongator dependent modification of U34 in the anticodon. Elongator deficiency resulted in lack of growth on medium lacking adenine and in growth on media containing the toxic arginine analog canavanine due to inefficient suppression of ochre stop codons either in the *ade2-1* or in the *can1-100* alleles. Hence growth phenotypes on Ade⁻ and canavanine-containing media were complementary. Almost all mutants showed decreased tRNA modification activity, and we therefore concluded that both dimerization and iron-sulfur cluster coordination are essential for the catalytic activity of Elongator *in vivo* (Fig. 2d).

If DmcElp3 bound SAM in a similar fashion as in other known SAM domains, the iron cluster coordination loop would have to undergo a structural rearrangement (Fig. 1b). For this reason, it remains to be shown where SAM exactly binds, if it involves the third highly conserved cysteine residue (C23) and by which mechanism the 5'-deoxyadenosyl radical (5'-dA•) is generated and inertly transferred to the spatially distinct acetyl-CoA binding site to create an acetyl radical10.

We have used small-angle X-ray scattering (SAXS) to analyze if SAM and KAT domains of DmcElp3 were in a similar compact conformation in solution and if acetyl-CoA or SAM had any influence on their arrangement. As the theoretical scattering curves (based on the crystal structure) matched the experimentally determined curves very well and the radii of gyration almost perfectly matched the estimated values for the DmcElp3 monomers and dimers, we believe that the almost identical spatial arrangement of DmcElp3 can also be found in solution (Supplementary Fig. 2e). As we did not observe any changes of the scattering profiles in the presence of acetyl-CoA or SAM to the dimer and monomer, we were certain that these ligands do not induce any major rearrangements of the domains (Supplementary Fig. 2f).

In our hands the incubation of anaerobically purified DmcElp3 with acetyl-CoA in the presence of $Na_2S_2O_4$ led to robust unspecific acetylation of several surface exposed lysine residues (e.g. K2, K266, K276 and K380). Strikingly, we observed unspecific acetylation of DmcElp3 mutants (e.g. Y441A, expected to be catalytically inactive) both, in their dimeric and monomeric forms, of *Methanocaldococcus infernus* Elp3 (MinElp3), and even of other unrelated proteins lacking HAT-like active sites or proven KAT activity (e.g. BTG12, Kti13) upon their incubation with acetyl-CoA in the presence of $Na_2S_2O_4$ (Supplementary Fig. 3a). This chemical side reaction prevented us from reliably testing the activity of DmcElp3 in a recently established *in vitro* tRNA modification assay10 (see also Supplementary Note 2). We have therefore focused on characterizing the initial steps of the proposed modification reaction cycle that precede the proposed radical mechanism.

tRNA binds to the interface of the KAT and SAM domain

Firstly, we tested DmcElp3 for tRNA binding using radioactive electrophoretic mobility shift assays (EMSA). *In vitro* transcribed tRNA$_{Glu}$^{UUC} from *D. mccartyi* and *S. cerevisiae* bound directly to monomeric and dimeric DmcElp3 with comparable affinities (K$_d$ of ~4 μM; Supplementary Fig. 3b). By analyzing conservation and surface charge of DmcElp3 a highly conserved basic cavity located between the SAM and KAT domains immediately caught our attention (Supplementary Fig. 3c). We subsequently mutated all conserved basic residues in the proximity of this region to map the tRNA binding region at the single residue level. Mutating residues in the center of the patch (K229A, R274A, R277A, R280A, R314A) clearly reduced tRNA binding (Fig. 3a,b). Other residues that were in close proximity affected tRNA binding to a lesser extent (K77, H73, R155, K193; Fig. 3b and Supplementary Fig. 4a). Though, double mutations R49A R64A, R155A K193A, K229A R277A and R274A R314A enhanced the effects of the respective individual mutations (Fig. 3c). In addition, we analyzed a region of three highly conserved basic residues in the N-terminus, which was located very close to the mapped tRNA binding site. After deletion of this stretch (DmcElp3$_{9-459}$) or substitutions (K2A K3A, R6A) the tRNA binding to DmcElp3 was fully abolished (Fig. 3c). This extended region, which contained additional stretches of basic residues in archaea and eukaryotes (Fig. 1d), was disordered in our crystal structure and might undergo structural rearrangements upon tRNA recruitment. Mutations of conserved residues distant from the mapped tRNA binding site, like in the dimerization interface (K26A, C27S C30S, Y40A, H73A, R136A, R173A, Y231A) or the acetyl-CoA binding pocket (E386A, E386A H388A, Y441A), gave no decrease in tRNA affinity (Supplementary Fig. 4a,b). Mutations affecting tRNA binding *in vitro* were introduced into ScElp3 and tested for tRNA modification activity *in vivo*. The phenotypes were comparable to that of the *elp3* deletion strain (Fig. 3d,e and Supplementary Fig. 4c). Therefore, tRNA recruitment is essential for proper tRNA modification but independent from iron-sulfur cluster coordination, SAM or acetyl-CoA binding. Differences for the N-terminal mutations (K86A K88A, R91A) between the toxin and individual tRNA suppression assays may indicate specific importance of these residues for different tRNA species (Fig. 3d,e). Other eukaryotic and archaeal Elp3s possess additional non-conserved basic residues in their extended N-termini (Fig. 1d). We have mutated all lysine residues in the N-terminus of ScElp3 (K53A, K56A, K57A, K59A, K61A, K65A, K78A, K79A) to investigate their functional role in Elongator activity (Supplementary Fig. 4d). Consistent with their weak evolutionary conservation, the respective mutants fully conferred tRNA modification activity *in vivo*. Therefore, most basic residues in the extended N-terminus of ScElp3 seem to be dispensable for Elongator's activity in yeast whereas the three conserved basic residues K2, K3, and R6A involved in tRNA binding in DmcElp3 were also important for tRNA modification in yeast.

Model of the DmcElp3–tRNA complex

We next characterized the interaction of DmcElp3 with tRNA$_{Glu}$ using single-strand specific RNase footprinting analyses. The binding of DmcElp3 mainly protected two regions of the tRNA, namely the anticodon loop and the D-loop (Fig. 4a,b). The unexpected protection of the D-loop explains why the anticodon loop, carrying the modifiable uridine base, is not sufficient by itself for binding to DmcElp3 (data not shown). Strong band intensities were

also visible in the variable loop after DmcElp3 binding. However, these bands were also present in the control lane and most likely resulted from a rearrangement of this region upon DmcElp3 binding. Using our biochemical restraints, we were able to specifically place a tRNA molecule into the composite active site formed by the SAM and KAT domains, providing a model of the initial tRNA recruitment step. Strikingly, this approach positioned the modifiable wobble base in close proximity to the active center of the KAT domain and the D-loop in proximity of the flexible N-terminal stretch important for tRNA binding, which probably discriminates for binding of only properly folded tRNAs (Fig. 3c, Fig. 4b,c).

Regulation of acetyl-CoA binding to DmcElp3

During the structural comparison with different HAT domains, we observed that a loop region in DmcElp3 (residues 390 to 407) occupied the canonical acetyl-CoA binding site (Fig. 1a). Replacing the loop with a short linker led to the 4-fold increase in affinity for tRNA (K_d of ~1 μM; Supplementary Fig. 5a). We therefore concluded that incipient tRNA binding led to the displacement of the loop region and initiated productive acetyl-CoA binding, thereby explaining why the acetyl-CoA turnover was strongly stimulated in the presence of tRNAs[10]. We were able to determine the crystal structure of the DmcElp3 390–407$_{GSGSG}$ in the presence of acetyl-CoA at 2.6 Å resolution (Supplementary Fig. 5b). We only found weak electron density for CoA in our crystal structure, presumably because the ligand, in the absence of tRNA, was too flexible to reliably assess its detailed binding mode. Nevertheless, we were able to show that the opening of this cleft did not lead to overall rearrangements in DmcElp3 (Supplementary Fig. 5c) and that the wobble base position of the docked tRNA would perfectly align with the bound position of the acetyl group in acetyl-CoA (Fig. 4d). On the basis of our results, we propose that recruitment of tRNA by DmcElp3 ensures productive binding of acetyl-CoA in the otherwise blocked canonical binding site which in turn leads to activation of the latter and the addition of the activated acetyl-CoA group to wobble base uridines before acetyl-CoA hydrolysis. In addition, our results demonstrated that the Elp3 domain architecture is essential for specifically recognizing tRNAs and simultaneously blocks the binding of unspecific substrates (e.g. peptides) to avoid undesirable or off-target acetylation by the created acetyl radical intermediate.

Model of the Elp3 mediated cm^5 modification reaction

Above we have shown that specific regions in the SAM and KAT domains of DmcElp3 contribute to activity of Elp3 and how it recognizes tRNAs. In an attempt to explain the necessary steps of the modification reaction, in the context of our structural data and the proposed reaction cycle by Huang and colleagues[10], we investigated necessary movements of specific small loop regions in homology to the structure of iron sulfur cluster containing SAM domain of RlmN bound to SAM. Firstly, we realized that mainly two regions (aa19-55 and aa161-176) would have to undergo structural rearrangements to bring the iron sulfur cluster in closer proximity of the tRNA and acetyl-CoA binding site. After this movement it is likely that the third conserved cysteine residue is involved in cluster coordination and SAM could be recruited to produce the necessary 5'-dA• (Fig. 5a) and the dimer is maintained by residues not directly involved in cluster coordination (e.g. R136, R173). As the dimer bound tRNA with the same affinity as the monomer we believe that this process is

independent of tRNA binding, which involved highly conserved basic residues in the central cavity between SAM and KAT domains. Though, tRNA binding facilitated the displacement of the acetyl-CoA blocking loop and the binding and hydrolysis of acetyl-CoA (Fig. 5b). From our structure we can deduct that only relatively small movements in Elp3 would bring the necessary components, namely 5'-dA•, acetyl-CoA and U34, in close proximity of each other (Fig. 5c). Although, our results provide the first structural insights into this complicated modification, it will take additional structural and biochemical analyses to understand the individual reaction steps in greater detail.

Mapping disease related mutations in Elp3

Finally, our structural results also allowed us to precisely locate mutations that have been previously identified by different groups[9–11,20,21,47–51] and cancer sequencing projects (Supplementary Fig. 6 a,b). Interestingly, two Elp3 mutations (R456K, R475K), identified by a mutagenesis screen for synaptic transmission and neuronal survival in flies[16], are located at the interface of the KAT and SAM domains, probably promoting neurodegenerative phenotypes by causing destabilization and malfunction of Elp3. We have analyzed several mutations related to neurodegenerative diseases (D322N, R463K, R484K) or cancer (R413T, D454N, R433K) by mutating equivalent residues in *S. cerevisiae ELP3* and testing for functionality. Interestingly, five of the six mutations (D322N, R463K, R484K, R413T, R433K) fully or partially phenocopy an *elp3* deletion strain (Supplementary Fig. 6c) suggesting dysfunctional Elongator complex in these patients. Our work therefore not only provides mechanistic insights into the initial steps of the tRNA modification reaction, but also a framework for further functional studies that will clarify the contribution of mutations in Elp3 in neurodegenerative diseases and cancer.

Discussion

In this study we provide molecular and functional insight into the yet poorly characterized Elp3 subunit, which harbors the catalytic center for the tRNA modification reaction. The relative arrangement of the two domains in Elp3 spatially restricts the binding of peptides to the acetyl-transfer region in the KAT domain while it allows the wobble base of a bound tRNA to specifically access this active site. In addition, we observed a [Fe–S] cluster located in the interface of two DmcElp3 molecules, which formed dimers in solution and in our crystals. In eukaryotes, Elongator forms a multi-subunit complex and we previously showed that the fully assembled endogenous Elongator complex of *S. cerevisiae* contains two copies of each its subunits[25], including two Elp3 molecules. Therefore, the five other Elongator subunits (Elp1, Elp2, Elp4, Elp5, Elp6) could provide a suitable scaffold to stabilize the interaction of two Elp3 molecules in eukaryotes. The presence of these other subunits could have led to a decreased selective evolutionary pressure in eukaryotes to conserve a stable Elp3 dimer interface.

We do appreciate that the location and coordination of the [Fe–S] cluster in DmcElp3 is unexpected and different from other known radical SAM enzymes[52]. Therefore, our structural snapshot cannot fully explain the suggested SAM-mediated radical based modification mechanism[10]. Although DmcElp3 is annotated as a SAM radical enzyme, it is

clear from our analysis that it is not a classical member of this family. Our results show that DmcElp3 can form dimers and monomers, where the latter are colorless and do not yield EPR signals. At present, we cannot fully exclude that DmcElp3 monomers harbor a highly sensitive [Fe–S] cluster presumably employing the conserved residue C23, which in our structure is not involved in [Fe–S] coordination. Nevertheless, in our analyses under aerobic and anaerobic conditions [Fe–S] coordination is strongly stabilized by DmcElp3 dimerization. Despite intense efforts, no crystals were obtained during co-crystallization attempts of anaerobically and aerobically purified DmcElp3 (monomer and dimer) in the presence of acetyl-CoA, CoA, SAM, different *in vitro* transcribed full-length tRNAs from *D. mccartyi* and combinations thereof.

However, we determined the crystal structure of a deletion construct, lacking a previously uncharacterized loop region that specifically blocked the predicted acetyl-CoA binding site in the KAT domain, in the presence of acetyl-CoA. Interestingly, the deletion of this loop resulted in an increased affinity for tRNA suggesting a direct mechanistic connection between tRNA binding and acetyl-CoA recruitment. tRNA binding seems to precede acetyl-CoA binding, which provides a possible explanation for the partial flexibility of acetyl-CoA in the absence of substrate tRNA. In addition, we were able to map the tRNA binding site using structure-guided mutational approaches and RNase protection assays. Strikingly, our resulting model of tRNA-bound Elp3 located the wobble base position in close proximity to the active site of the KAT domain. Therefore, we conclude that the domain architecture of Elp3 allows specific recognition of tRNAs by the SAM domain and subsequent transfer of an activated acetyl-group from acetyl-CoA bound in the KAT domain.

As DmcElp3 shows very high sequence similarity to Elp3 from different organisms we are also able to locate most of the previously published mutations in our structure and provide a structural framework for their dysfunction. In addition, we have tested several disease- and cancer-related mutations in yeast and show that they affect the tRNA modification activity of Elongator, suggesting a direct correlation of Elp3 dysfunction with disease progression.

Online Methods

Cloning of the *DmcELP3* gene from *D. mccartyi*

Genomic DNA of *Dehalococcoides mccartyi* strain CBDB1 was provided by Prof. G. Sawers (Martin-Luther-University Halle). The open reading frame of *DmcELP3* (cbdbA595) was amplified and cloned into plasmid pRZ4857 to give pRZ51.

Aerobic protein expression and purification

The DmcElp3 codon sequence was subcloned into the pETM30 vector to obtain N-terminally 6xHis-GST-tagged proteins and transformed into BL21 pSarRare *E. coli*. Cultures were grown at 37°C until OD_{600} ~1, protein expression was induced using 0.5 mM isopropyl-β-D-thiogalactopyranoside (IPTG), incubated at 18°C overnight and harvested the next morning by centrifugation. Pellets were resuspended in lysis buffer (50 mM HEPES pH 7.5, 300 mM NaCl, 20 mM imidazole, 1 mM $MgCl_2$, 5% glycerol, 2 mM β-mercaptoethanol, protease inhibitor tablets (Roche), DNase and lysozyme) and lysed using a

high pressure homogenizer. The lysate was cleared by centrifugation at 15,000 g for 1 h at 4°C and the supernatant was incubated with NiNTA resin for 2 h at 4°C. The bound protein was washed with wash buffer (50 mM HEPES pH 7.5, 300 mM NaCl, 1 mM $MgCl_2$, 5% glycerol, 2 mM β-mercaptoethanol) and eluted with elution buffer (50 mM Tris pH 7.5, 300 mM NaCl, 250 mM imidazole, 1 mM β-mercaptoethanol). Subsequently, the eluted protein was dialyzed (20 mM HEPES pH 7.5, 300 mM NaCl, 20 mM imidazole, 1 mM β-mercaptoethanol) in the presence of TEV protease at 4°C overnight. The cleaved tag was removed using a second NiNTA step and flow-through was applied to a S200 (26/60) gel filtration column (GE Healthcare) equilibrated in gel filtration buffer (20 mM HEPES pH 7.5, 150 mM NaCl, 5 mM DTT). Fractions were analyzed by SDS-PAGE, pooled and concentrated. Single amino acid substitutions were generated using the Quikchange mutational kit (Agilent Technologies). All mutant proteins were expressed and purified like the wild type protein. Uncropped images of all used gels and autoradiographs are shown in Supplementary data set 1.

Crystallization and Structure determination

Native and selenomethionine substituted crystals were grown at 18°C using the hanging drop vapor diffusion method. Purified DmcElp3 protein in gel filtration buffer was concentrated to 10 mg/ml and combined with equal volume of 100 mM MES pH 6.3 and 4% PEG 4000. Crystals grew until day 7, were cryo-protected with 30% glycerol and subsequently flash frozen in liquid nitrogen. Native and selenomethionine data sets for DmcElp3 were collected at ESRF beamline ID29 on a Pilatus 6M-F detector. The DmcElp3 selenomethionine crystals diffracted to higher resolution than the native crystals and the selenomethionine data set was therefore used for the refinement. Data processing was performed using XDS58. SAD phases were calculated from identified selenium sites using autoSHARP59. The resulting electron density map after solvent flattening was of good quality and an initial model was built and subsequently refined using Phenix60. DmcElp3 390-407$_{GSGSG}$ crystals were obtained under the same crystallization condition but by premixing purified protein with 5 mM acetyl-CoA (Sigma). The structure was solved using Phaser61 and refined using Phenix. The refinement statistics of the respective models are given in (Table 1). The geometry of the models was validated using Molprobity62. Model figures and superimpositions were prepared using Pymol (http://www.pymol.org) and Coot63. For the prediction of movements within DmcElp3 loop regions, different models of the DmcElp3 cluster coordination region were created using I-TASSER64 and PHYRE65 servers using different RlmN templates (PDB IDs 3RFA36, 3RF936, 4PL166, 4PL266) and manually curated for necessary structural rearrangements. The [4Fe4S] cluster and bound SAM molecule were placed in accordance with their position in PDB ID 3RFA. tRNA was docked using HADDOCK67 with subsequent manual refinement.

Anaerobic protein expression and purification

The *D. mccartyi* 6xHis-DmcElp3 or 6xHis-GST-DmcElp3 were expressed in of BL21-codon plus(DE3)-RIL under the control of the T7 promoter together with the *Azotobacter vinelandii isc* operon under control of an arabinose-inducible promoter. Cells were grown in 1 L LB medium at 37°C. At OD_{600} of 0.3, arabinose was added to the final concentration of 0.05 % (w/v). At OD_{600} of 0.6, the cultures were cooled down to 18°C and supplemented

with $FeCl_3$, $Fe(NH_4)_2(SO_4)_2$ and L-cysteine to final concentrations of 50 µM, 50 µM and 400 µM, respectively. Expression of DmcElp3 was induced by 0.1 mM IPTG, and the flasks were sealed to limit the amount of oxygen in the system and incubated for ~20 h at 18°C.

Harvested cells were resuspended in 30 ml of lysis buffer (200 mM Tris-HCl pH 7.5, 150 mM NaCl, 10 mM $MgCl_2$, 5 mM imidazole and 1 mM DTT). After addition of lysozyme (45 mg) and benzonase (20 U/ml of lysis buffer) the cells were incubated at room temperature for 1h. The mixture was frozen in liquid nitrogen, thawed at 25°C and cell debris was removed by centrifugation at 14,000 g for 45 min. The concentration of NaCl in the supernatant was adjusted to 500 mM and it was applied on 500 µl of Ni-NTA agarose resin (Qiagen) pre-equilibrated on Poly-Prep chromatography column (BioRad) with the lysis buffer containing 500 mM NaCl. Subsequently, the resin was washed with 1x10ml of equilibration buffer and with 2x10ml of the same buffer containing 20 mM imidazole. The protein was eluted with 200 mM Tris-HCl pH 7.5, 500 mM NaCl, 250 mM imidazole and 1 mM DTT in 0.5-1 ml fractions. The fractions exhibiting dark red/brown color were applied on PD10 column (GE Healthcare) and eluted with 100 mM HEPES pH 7.5, 100 mM NaCl, 1 mM DTT buffer. The proteins were quantified using Bio-Rad Protein Assay, concentrated, if desired, using Amicon-Ultra 0.5 ml centrifugal filters (Millipore), aliquoted and frozen in liquid nitrogen. All the steps except centrifugation were performed anaerobically under argon in a sealed chamber.

Yeast Strains and Manipulation

S. cerevisiae strains are listed in the Supplementary Table 1. The parent strain for *elp3* point mutants was the *elp3* strain ONY14 derived from UMY 2893 by replacement of the *ELP3* open reading frame with the marker gene *KlURA3* from *Kluyveromyces lactis*. *elp3* mutant strains RZY63-RZY75, RZY90, RZY91, RZY116, RZY119-RZY130, and RZY137 were generated by primer directed mutagenesis: genomic DNA from yeast strain CMY54 (*ELP3-(myc)$_3$::SpHIS5*) was used as a template to generate (myc)$_3$-epitope tagged *elp3* mutated PCR fragments. The *elp3-(cmyc)$_3$::SpHIS5* fragments containing the indicated mutations were transformed into ONY1468 and transformants were selected for histidine prototrophy and loss of the *KlURA3* marker (by 5-fluoroorotic acid resistance). The correct replacement of the *URA3* knockout cassette by the mutagenized *elp3* alleles was verified by PCR using primer pair Elp3-370-Fw/Elp3-400-Rv. Yeast strains ONY21, ONY22 and ONY24 containing untagged mutagenized *elp3* alleles were similarly generated by PCR from *ELP3* plasmid and introduced into strain ONY14. Correct replacements of the *elp3::KlURA3* cassette by the respective *elp3* alleles were verified by PCR and all mutations by DNA sequencing.

Plasmid constructs

Plasmid carrying the *ScELP3-(myc)$_3$* gene and mutated alleles are based on the centromeric plasmid p424TDH69. The gene was amplified by PCR from genomic DNA using yeast strain FFY3t (*ELP3-(myc)$_3$::SpHIS5*) as a template. The PCR fragment was cloned into p424TDH using *Eco*RI and *Xho*I to give pON34 (*ELP3-(myc)$_3$*). pON34 served as a template to generate mutated *elp3-(myc)$_3$* alleles by using Quikchange Site-Directed-Mutagenesis Kit (Agilent Technologies) to construct the following plasmids: pON71 (*elp3-*

H110A-(myc)₃), pON72 (*elp3-C118A/C121A-(myc)₃*), pON73 (*elp3-V119A/Y120A-(myc)₃*), pON74 (*elp3-Y136A-(myc)₃*), pON75 (*elp3-R232A-(myc)₃*), pON76 (*elp3-R269A-(myc)₃*), pON77 (*elp3-H271A-(myc)₃*) and pON78 (*elp3-W341A-(myc)₃*).

Phenotypical Analyses of Mutants

To analyze the function of mutated *elp3* alleles, the γ-toxin sensitivity was assayed as described before[70]. Responses of yeast cells to intracellular expression of zymocin lethal tRNase γ-toxin subunit involved the galactose inducible *GAL1*-γ-toxin expression plasmid pLF1671. Transformed strains were spotted in 10-fold serial cell dilutions on either 2% dextrose (repressing conditions) or 2% galactose (inducing conditions) containing plates and were incubated for 3 days at 30°C. To analyze the effect of *elp3* mutations on ochre stop codon suppression by suppressor tRNA *SUP4* was carried out as described previously[72]. Yeast strains based on UMY2893 (*ade2-1 can1-100)* were spotted on plates lacking adenine or containing the toxic arginine analogue canavanine. When the *SUP4* tRNA is nonfunctional, e.g. because it lacks the Elongator dependent uridine modification strains cannot grow in absence of adenine but are resistant against canavanine. Plates were analyzed after incubation at 30°C for 4 days.

Spectroscopic analyses of DmcElp3

The UV-VIS spectroscopic analysis of anaerobically purified DmcElp3 was performed at room temperature in quartz cuvettes in a total volume of 0.5 ml using a Carry 50 Bio UV/visible Spectrophotometer (Varian Inc.). The 8 μM DmcElp3 was analyzed in 100 mM Tris-HCl pH 7.5, 100 mM NaCl, 1 mM DTT buffer. The reduction was performed by addition of sodium dithionite to the final concentration of 1 mM. All the components were assembled anaerobically under argon in a cuvette that was subsequently sealed carefully with plastic wrap before transferring it to the spectrophotometer.

EPR spectra were recorded on a Bruker ElexSys X-band spectrometer fitted with an Oxford Instrument He-cryostat and temperature control system. The aerobically or anaerobically purified DmcElp3 at ~100 μM was analyzed in 20 mM HEPES pH 7.5, 150 mM NaCl and 5 mM DTT buffer in oxidized or reduced state. Samples were reduced by addition of 5 mM dithionite (from a stock solution at 1 M CAPS pH 10 buffer). Additions of the reducing agent was performed under argon at room temperature followed by vortexing and freezing of the sample in liquid nitrogen within 5 min after addition.

Thermofluor analyses DmcElp3 Mutants

Thermostability of purified DmcElp3 proteins was analyzed using thermofluor technology[73]. In detail, 20-50 μM of purified protein was incubated with SYPRO Orange in 20 mM HEPES pH 7.5, 150 mM NaCl and 5 mM DTT. Using a StepOne Plus Real-Time PCR system (Applied Biosystems) the samples were subjected to a temperature gradient from 20°C to 95°C (over the period of 2 h) while simultaneously measuring the emitted fluorescence signal (λ = 590 nm).

SAXS

SAXS data for DmcElp3 was acquired at beamline BM29 at ESRF, Grenoble. DmcElp3 monomer and dimer species were separated by gel filtration and were subsequently concentrated. Serial dilutions were measured at 20°C in 20 mM HEPES 7.5, 150 mM NaCl, 5mM DTT buffer. DmcElp3 dimer was measured at 4.34, 2.17, 1.08 and 0.54 mg/ml, while Elp3 monomer was measured at 2.34, 1.16, 0.58 and 0.29 mg/ml. For binding with acetyl-CoA and SAM, a large excess (10-80x molar equivalents across the concentration range) was added to the samples and buffers in order to obtain an accurate buffer subtraction. Each dataset was acquired using 10 frames and 100% transmission with a 3 second exposure per frame. Frames were then compared for radiation damage using CORMAP[74], averaged accordingly and buffer subtracted. In order to minimize the interparticle effects, the ATSAS package PRIMUS[75] was used to extrapolate the concentration series to infinite dilution, yielding data in agreement with monodisperse monomer and dimer populations for each concentration series. Comparison of experimental data to theoretical scattering curves was done using CRYSOL[75].

EMSA

Nucleic acids were 5'-labeled (^{32}P and T4 PNK) or 3'-labeled (^{32}pCp and T4 RNA Ligase) and gel purified on denaturing 15% urea-PAGE. Radioactively labeled tRNA was first renatured by heating in annealing buffer (20 mM HEPES pH 7.5, 50 mM NaCl, 50 mM KCl) at 80°C for 5 min, slowly cooled down to 25°C and diluted with 20 mM HEPES pH 7.5, 150 mM NaCl, 5 mM DTT, 1 mM MgCl$_2$. To quantify binding of DmcElp3 to *D. mccartyi* tRNA$_{Glu-1}$ (5'-GCCCCCATCGTCTAGAGGCccAGGACAGCGGCCTTTCACGCCGTCAACAGGGGTT CGAATCCCCCTTGGGGGGTACCA-3'), proteins were serially diluted, followed by the addition of renatured ^{32}P-labeled RNA (~ 5000 cpm). After incubation at 25°C for 15 min, the reactions were loaded on a 6% native gel. The gels were dried and subsequently analyzed by detection on film.

RNase Protection Assay

Enzymatic digestions were performed on 3' or 5' end-labelled tRNA (~50,000 cpm). Prior to modification, the tRNA was denatured in double-distilled water for 2 min at 60°C, quickly cooled on ice (2 min), then slowly brought back to RT (20 min) in 50 mM sodium cacodylate buffer (pH 7.5), 5 mM MgCl$_2$, 0.1 M KCl, 5 mM DTT. If the tRNA was probed with protein, 20 μM DmcElp3 was added to the refolded tRNA in the same buffer and the complex was formed for 15 min at RT. Enzymatic probing was carried out with nuclease S1 (32 kDa) which is specific for single-stranded structures without base specificity, RNase T1 (11 kDa) specific for G in single-stranded RNA, and RNase T2 (36 kDa) specific for single stranded nucleotides with a preference for A nucleotides. Digestion with RNase T1 (0.5 or 1 unit), RNase T2 (1 or 2 U) or nuclease S1 (3 or 6 U) was accomplished by incubation for 10 min at RT. For nuclease S1, the reaction was supplemented with 0.2 mM ZnCl$_2$. For each reaction, a control (C) without RNase was treated in parallel. After phenol extraction and ethanol precipitation, the samples were analyzed on denaturing 12% PAGE.

Supplementary Material

Refer to Web version on PubMed Central for supplementary material.

Acknowledgement

References

1. Fredrick K, Ibba M. How the sequence of a gene can tune its translation. Cell. 2010; 141:227–9. [PubMed: 20403320]

2. Pechmann S, Frydman J. Evolutionary conservation of codon optimality reveals hidden signatures of cotranslational folding. Nat Struct Mol Biol. 2013; 20:237–43. [PubMed: 23262490]

3. Komar AA. A pause for thought along the co-translational folding pathway. Trends Biochem Sci. 2009; 34:16–24. [PubMed: 18996013]

4. Thanaraj TA, Argos P. Ribosome-mediated translational pause and protein domain organization. Protein Sci. 1996; 5:1594–612. [PubMed: 8844849]

5. Rezgui VA, et al. tRNA tKUUU, tQUUG, and tEUUC wobble position modifications fine-tune protein translation by promoting ribosome A-site binding. Proc Natl Acad Sci U S A. 2013; 110:12289–94. [PubMed: 23836657]

6. Vendeix FA, et al. Human tRNA(Lys3)(UUU) is pre-structured by natural modifications for cognate and wobble codon binding through keto-enol tautomerism. J Mol Biol. 2012; 416:467–85. [PubMed: 22227389]

7. Nedialkova DD, Leidel SA. Optimization of Codon Translation Rates via tRNA Modifications Maintains Proteome Integrity. Cell. 2015; 161:1606–18. [PubMed: 26052047]

8. Glatt S, Muller CW. Structural insights into Elongator function. Curr Opin Struct Biol. 2013; 23:235–42. [PubMed: 23510783]

9. Huang B, Johansson MJO, Bystrom AS. An early step in wobble uridine tRNA modification requires the Elongator complex. RNA. 2005; 11:424–436. [PubMed: 15769872]

10. Selvadurai K, Wang P, Seimetz J, Huang RH. Archaeal Elp3 catalyzes tRNA wobble uridine modification at C5 via a radical mechanism. Nat Chem Biol. 2014; 10:810–2. [PubMed: 25151136]

11. Chen C, Huang B, Anderson JT, Bystrom AS. Unexpected accumulation of ncm(5)U and ncm(5)S(2) (U) in a trm9 mutant suggests an additional step in the synthesis of mcm(5)U and mcm(5)S(2)U. PLoS One. 2011; 6:e20783. [PubMed: 21687733]

12. Esberg A, Huang B, Johansson MJO, Bystrom AS. Elevated levels of two tRNA species bypass the requirement for elongator complex in transcription and exocytosis. Mol Cell. 2006; 24:139–148. [PubMed: 17018299]

13. Beck M, et al. The quantitative proteome of a human cell line. Mol Syst Biol. 2011; 7:549. [PubMed: 22068332]

14. Walker J, et al. Role of elongator subunit Elp3 in Drosophila melanogaster larval development and immunity. Genetics. 2011; 187:1067–75. [PubMed: 21288872]

15. Chen CC, Tuck S, Bystrom AS. Defects in tRNA Modification Associated with Neurological and Developmental Dysfunctions in Caenorhabditis elegans Elongator Mutants. PLoS Genet. 2009; 5:e1000561. [PubMed: 19593383]

16. Simpson CL, et al. Variants of the elongator protein 3 (ELP3) gene are associated with motor neuron degeneration. Hum Mol Genet. 2009; 18:472–481. [PubMed: 18996918]

17. Mehlgarten C, et al. Elongator function in tRNA wobble uridine modification is conserved between yeast and plants (vol 76, pg 1082, 2010). Mol Microbiol. 2010; 77:531–531.

18. Chen YT, et al. Loss of Mouse Ikbkap, a Subunit of Elongator, Leads to Transcriptional Deficits and Embryonic Lethality That Can Be Rescued by Human IKBKAP. Mol Cell Biol. 2009; 29:736–744. [PubMed: 19015235]

19. Slaugenhaupt SA, et al. Tissue-specific expression of a splicing mutation in the IKBKAP gene causes familial dysautonomia. Am J Hum Genet. 2001; 68:598–605. [PubMed: 11179008]

20. Wittschieben BO, et al. A novel histone acetyltransferase is an integral subunit of elongating RNA polymerase II holoenzyme. Mol Cell. 1999; 4:123–128. [PubMed: 10445034]

21. Paraskevopoulou C, Fairhurst SA, Lowe DJ, Brick P, Onesti S. The elongator subunit Elp3 contains a Fe4S4 cluster and binds S-adenosylmethionine. Mol Microbiol. 2006; 59:795–806. [PubMed: 16420352]

22. Lemmens R, Moore MJ, Al-Chalabi A, Brown RH Jr, Robberecht W. RNA metabolism and the pathogenesis of motor neuron diseases. Trends Neurosci. 2010; 33:249–58. [PubMed: 20227117]

23. Xu H, et al. Dimerization of elongator protein 1 is essential for Elongator complex assembly. Proc Natl Acad Sci U S A. 2015; 112:10697–702. [PubMed: 26261306]

24. Dong C, et al. The elp2 subunit is essential for elongator complex assembly and functional regulation. Structure. 2015; 23:1078–86. [PubMed: 25960406]

25. Glatt S, et al. The Elongator subcomplex Elp456 is a hexameric RecA-like ATPase. Nat Struct Mol Biol. 2012; 19:314–20. [PubMed: 22343726]

26. Lin Z, et al. Crystal structure of elongator subcomplex Elp4-6. J Biol Chem. 2012; 287:21501–8. [PubMed: 22556426]

27. Glatt S, et al. Structure of the Kti11/Kti13 heterodimer and its double role in modifications of tRNA and eukaryotic elongation factor 2. Structure. 2015; 23:149–60. [PubMed: 25543256]

28. Kolaj-Robin O, McEwen AG, Cavarelli J, Seraphin B. Structure of the Elongator cofactor complex Kti11/Kti13 provides insight into the role of Kti13 in Elongator-dependent tRNA modification. FEBS J. 2015; 282:819–33. [PubMed: 25604895]

29. Svejstrup JQ. Elongator complex: how many roles does it play? Curr Opin Cell Biol. 2007; 19:331–336. [PubMed: 17466506]

30. Versees W, De Groeve S, Van Lijsebettens M. Elongator, a conserved multitasking complex? Mol Microbiol. 2010; 76:1065–1069. [PubMed: 20398217]

31. Glatt S, Seraphin B, Muller CW. Elongator: transcriptional or translational regulator? Transcription. 2012; 3:273–276. [PubMed: 22889844]

32. Karlsborn T, Tukenmez H, Chen C, Bystrom AS. Familial dysautonomia (FD) patients have reduced levels of the modified wobble nucleoside mcmsU in tRNA. Biochem Biophys Res Commun. 2014; 454:441–445. [PubMed: 25450681]

33. Najmabadi H, et al. Deep sequencing reveals 50 novel genes for recessive cognitive disorders. Nature. 2011; 478:57–63. [PubMed: 21937992]

34. Loffler FE, et al. Dehalococcoides mccartyi gen. nov., sp. nov., obligately organohalide-respiring anaerobic bacteria relevant to halogen cycling and bioremediation, belong to a novel bacterial class, Dehalococcoidia classis nov., order Dehalococcoidales ord. nov. and family Dehalococcoidaceae fam. nov., within the phylum Chloroflexi. Int J Syst Evol Microbiol. 2013; 63:625–35. [PubMed: 22544797]

35. Seshadri R, et al. Genome sequence of the PCE-dechlorinating bacterium Dehalococcoides ethenogenes. Science. 2005; 307:105–8. [PubMed: 15637277]

36. Boal AK, et al. Structural basis for methyl transfer by a radical SAM enzyme. Science. 2011; 332:1089–92. [PubMed: 21527678]

37. Benitez-Paez A, Villarroya M, Armengod ME. The Escherichia coli RlmN methyltransferase is a dual-specificity enzyme that modifies both rRNA and tRNA and controls translational accuracy. RNA. 2012; 18:1783–95. [PubMed: 22891362]

38. Schwalm EL, Grove TL, Booker SJ, Boal AK. Crystallographic capture of a radical S-adenosylmethionine enzyme in the act of modifying tRNA. Science. 2016; 352:309–12. [PubMed: 27081063]

39. Dyda F, Klein DC, Hickman AB. GCN5-related N-acetyltransferases: a structural overview. Annu Rev Biophys Biomol Struct. 2000; 29:81–103. [PubMed: 10940244]

40. Creppe C, et al. Elongator Controls the Migration and Differentiation of Cortical Neurons through Acetylation of alpha-Tubulin. Cell. 2009; 136:551–564. [PubMed: 19185337]

41. Miskiewicz K, et al. ELP3 controls active zone morphology by acetylating the ELKS family member Bruchpilot. Neuron. 2012; 72:776–88. [PubMed: 22153374]

42. Sweeney WV, Rabinowitz JC. Proteins containing 4Fe-4S clusters: an overview. Annu Rev Biochem. 1980; 49:139–61. [PubMed: 6250442]

43. Lanciano P, et al. New method for the spin quantitation of [4Fe-4S](+) clusters with S = (3)/(2). Application to the FS0 center of the NarGHI nitrate reductase from Escherichia coli. J Phys Chem B. 2007; 111:13632–7. [PubMed: 17988112]

44. Conover RC, et al. Spectroscopic characterization of the novel iron-sulfur cluster in Pyrococcus furiosus ferredoxin. J Biol Chem. 1990; 265:8533–41. [PubMed: 2160461]

45. Bruska MK, Stiebritz MT, Reiher M. Analysis of differences in oxygen sensitivity of Fe-S clusters. Dalton Trans. 2013; 42:8729–35. [PubMed: 23632881]

46. Dong M, et al. Dph3 is an electron donor for dph1-dph2 in the first step of eukaryotic diphthamide biosynthesis. J Am Chem Soc. 2014; 136:1754–7. [PubMed: 24422557]

47. Jablonowski D, Zink S, Mehlgarten C, Daum G, Schaffrath R. tRNAGlu wobble uridine methylation by Trm9 identifies Elongator's key role for zymocin-induced cell death in yeast. Mol Microbiol. 2006; 59:677–88. [PubMed: 16390459]

48. Nelissen H, et al. The elongata mutants identify a functional Elongator complex in plants with a role in cell proliferation during organ growth. Proc Natl Acad Sci U S A. 2005; 102:7754–9. [PubMed: 15894610]

49. Greenwood C, Selth LA, Dirac-Svejstrup AB, Svejstrup JQ. An iron-sulfur cluster domain in Elp3 important for the structural integrity of elongator. J Biol Chem. 2009; 284:141–9. [PubMed: 18986986]

50. Okada Y, Yamagata K, Hong K, Wakayama T, Zhang Y. A role for the elongator complex in zygotic paternal genome demethylation. Nature. 2010; 463:554–8. [PubMed: 20054296]

51. Wittschieben BO, Fellows J, Du W, Stillman DJ, Svejstrup JQ. Overlapping roles for the histone acetyltransferase activities of SAGA and elongator in vivo. EMBO J. 2000; 19:3060–8. [PubMed: 10856249]

52. Wang JR, et al. Recent Advances in Radical SAM Enzymology: New Structures and Mechanisms. Acs Chemical Biology. 2014; 9:1929–1938. [PubMed: 25009947]

53. Clements A, et al. Structural basis for histone and phosphohistone binding by the GCN5 histone acetyltransferase. Mol Cell. 2003; 12:461–73. [PubMed: 14536085]

54. Rojas JR, et al. Structure of Tetrahymena GCN5 bound to coenzyme A and a histone H3 peptide. Nature. 1999; 401:93–8. [PubMed: 10485713]

55. Poux AN, Marmorstein R. Molecular basis for Gcn5/PCAF histone acetyltransferase selectivity for histone and nonhistone substrates. Biochemistry. 2003; 42:14366–74. [PubMed: 14661947]

56. Sekine S, Nureki O, Shimada A, Vassylyev DG, Yokoyama S. Structural basis for anticodon recognition by discriminating glutamyl-tRNA synthetase. Nat Struct Biol. 2001; 8:203–6. [PubMed: 11224561]

57. Glatt S, et al. Structure of the Kti11/Kti13 heterodimer and its double role in modifications of tRNA and eukaryotic elongation factor 2. Structure. 2015; 23:149–60. [PubMed: 25543256]

58. Kabsch W. Xds. Acta Crystallogr D Biol Crystallogr. 2010; 66:125–32. [PubMed: 20124692]

59. delaFortelle E, Bricogne G. Maximum-likelihood heavy-atom parameter refinement for multiple isomorphous replacement and multiwavelength anomalous diffraction methods. Macromolecular Crystallography, Pt A. 1997; 276:472–494.

60. Adams PD, et al. PHENIX: building new software for automated crystallographic structure determination. Acta Crystallogr D Biol Crystallogr. 2002; 58:1948–1954. [PubMed: 12393927]

61. McCoy AJ, et al. Phaser crystallographic software. J Appl Crystallogr. 2007; 40:658–674. [PubMed: 19461840]

62. Davis IW, et al. MolProbity: all-atom contacts and structure validation for proteins and nucleic acids. Nucleic Acids Res. 2007; 35:W375–W383. [PubMed: 17452350]

63. Emsley P, Cowtan K. Coot: model-building tools for molecular graphics. Acta Crystallogr D Biol Crystallogr. 2004; 60:2126–2132. [PubMed: 15572765]

64. Yang J, et al. The I-TASSER Suite: protein structure and function prediction. Nat Methods. 2015; 12:7–8. [PubMed: 25549265]

65. Kelley LA, Sternberg MJ. Protein structure prediction on the Web: a case study using the Phyre server. Nat Protoc. 2009; 4:363–71. [PubMed: 19247286]

66. Silakov A, et al. Characterization of a cross-linked protein-nucleic acid substrate radical in the reaction catalyzed by RlmN. J Am Chem Soc. 2014; 136:8221–8. [PubMed: 24806349]

67. van Zundert GC, et al. The HADDOCK2.2 Web Server: User-Friendly Integrative Modeling of Biomolecular Complexes. J Mol Biol. 2016; 428:720–5. [PubMed: 26410586]

68. Knop M, et al. Epitope tagging of yeast genes using a PCR-based strategy: more tags and improved practical routines. Yeast. 1999; 15:963–72. [PubMed: 10407276]

69. Mumberg D, Muller R, Funk M. Yeast vectors for the controlled expression of heterologous proteins in different genetic backgrounds. Gene. 1995; 156:119–22. [PubMed: 7737504]

70. Frohloff F, Fichtner L, Jablonowski D, Breunig KD, Schaffrath R. Saccharomyces cerevisiae Elongator mutations confer resistance to the Kluyveromyces lactis zymocin. EMBO J. 2001; 20:1993–2003. [PubMed: 11296232]

71. Jablonowski D, Zink S, Mehlgarten C, Daum G, Schaffrath R. tRNAGlu wobble uridine methylation by Trm9 identifies Elongator's key role for zymocin-induced cell death in yeast. Mol Microbiol. 2006; 59:677–88. [PubMed: 16390459]

72. Huang B, Johansson MJO, Bystrom AS. An early step in wobble uridine tRNA modification requires the Elongator complex. RNA. 2005; 11:424–436. [PubMed: 15769872]

73. Boivin S, Kozak S, Meijers R. Optimization of protein purification and characterization using Thermofluor screens. Protein Expr Purif. 2013; 91:192–206. [PubMed: 23948764]

74. Franke D, Jeffries CM, Svergun DI. Correlation Map, a goodness-of-fit test for one-dimensional X-ray scattering spectra. Nat Methods. 2015; 12:419–22. [PubMed: 25849637]

75. Petoukhov MV, et al. New developments in the program package for small-angle scattering data analysis. J Appl Crystallogr. 2012; 45:342–350. [PubMed: 25484842]
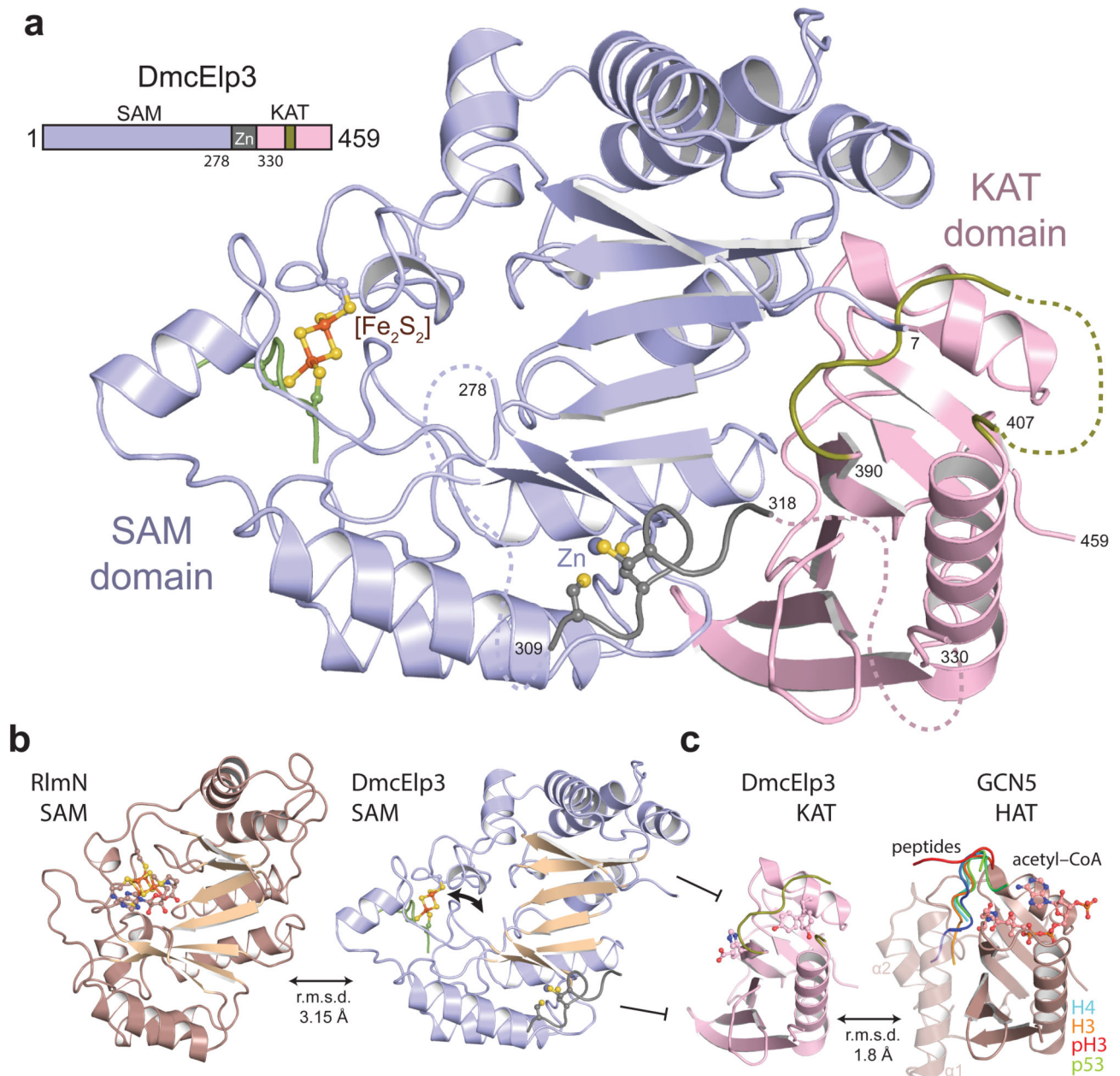
Figure 1. Crystal structure of DmcElp3.
(**a**) Overall structure of DmcElp3 shown in cartoon representation. Residue numbers are indicated and SAM domain (light blue), KAT domain (pink), iron cluster (orange and yellow), zinc binding loop (grey), and the acetyl-CoA blocking loop (olive) are highlighted. Disordered loops are shown by dotted lines. (**b**) Structural comparison of the SAM domains of DmcElp3 (right) and RlmN (left, PDB ID 3RFA36) showing the location of the iron-sulfur cluster and indicating its altered position in DmcElp3 (arrows). (**c**) Structural comparison of the KAT domains of DmcElp3 (left) and Gcn5 (right, PDB IDs 1Q2C (H4)53, 1QSN (H3)54, 1PUA (pH3)53 and 1Q2D (p53)55). Bound acetyl-CoA, substrate peptides and α1 and α2 helices are indicated.
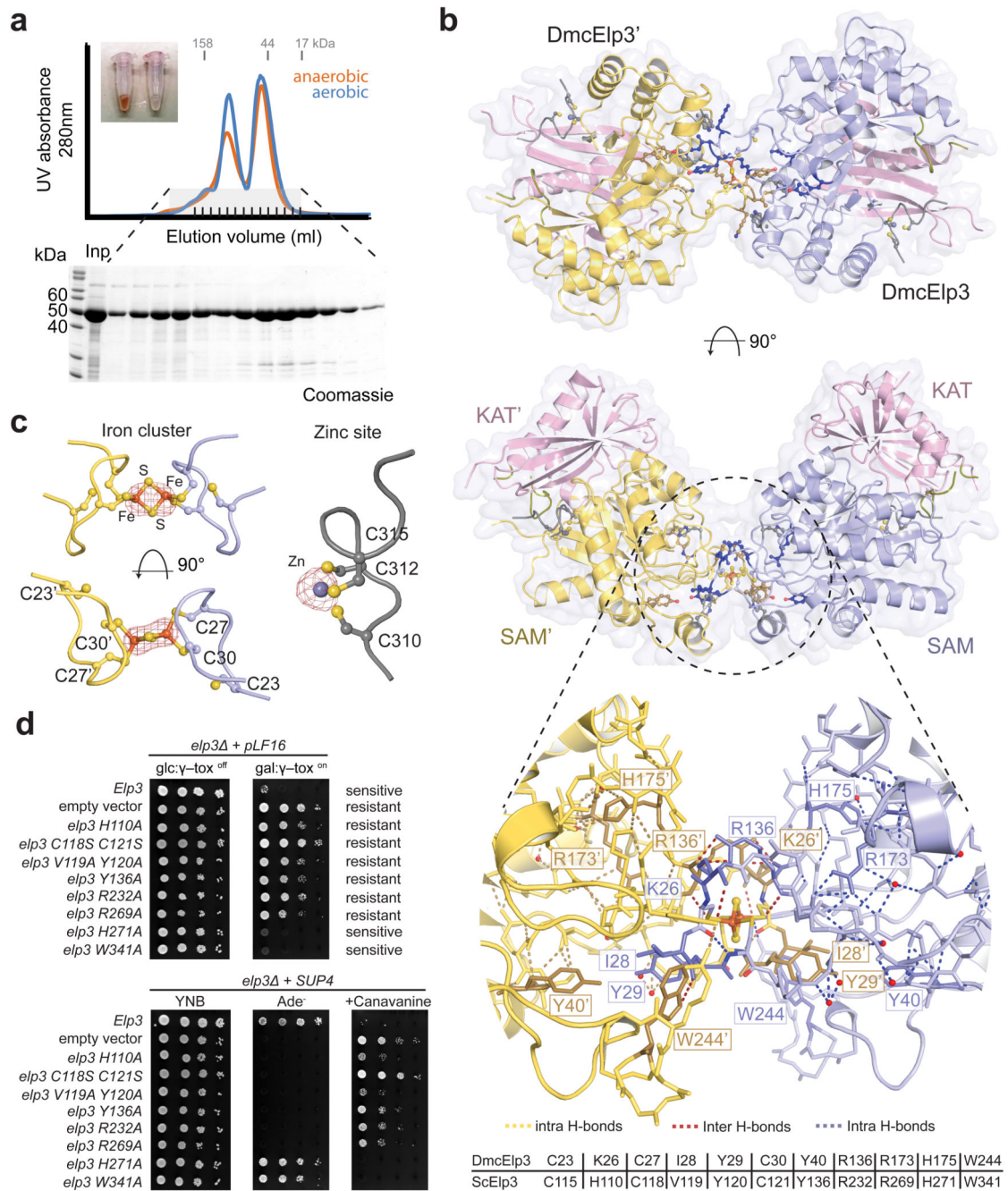
Figure 2. Dimerization of DmcElp3.

(**a**) Size exclusion chromatograms of aerobically (blue) and anaerobically (orange) purified wild type DmcElp3 (upper) and the SDS-PAGE gel of the corresponding fractions from the aerobically purified sample for crystallization. Concentrated protein solutions corresponding to dimeric and monomeric peaks of aerobically purified DmcElp3 are shown above. Elution position of reference proteins and their molecular mass are indicated (**b**) Overall structure of DmcElp3 in its dimeric conformation (top panel), showing DmcElp3 (light blue and pink) and its neighbouring dyad-related molecule of DmcElp3 (yellow and pink). Same as in top

panel, but 90° rotated view (middle panel). Close-up of the interaction interface showing hydrogen-bond networks and the involved residues (lower panel). (**c**) Anomalous difference Fourier maps calculated from a data set recorded close to the iron absorption edge (at 12 I/σ) (left) and close to the zinc absorption edge (at 7 I/σ) (right). (**d**) Phenotypes of yeast strains carrying the indicated *Scelp3* mutant alleles using γ toxin and *SUP4* suppression assays described in the text and detailed in Online Methods.

Figure 3. DmcElp3 tRNA interaction.
(**a**) Structure of DmcElp3 shown in cartoon representation showing the localization of tested mutants. Individual residues are shown in ball and sticks representation. Mutated residues with no decrease (green), decrease or decrease as double mutant (orange) and strong decrease (red) in tRNA binding are highlighted. (**b,c**) EMSA analysis of indicated point mutations using radioactively labelled tRNA and increasing amounts of protein (1.6, 7.5, 15 µM) on a 6% native Gel. Samples were also analysed using denaturing SDS-PAGE as loading control. (**d,e**) Phenotypes of yeast strains carrying the indicated *ScElp3* mutant

alleles using γ-toxin and SUP4 suppression assays described in the text and detailed in Online Methods.
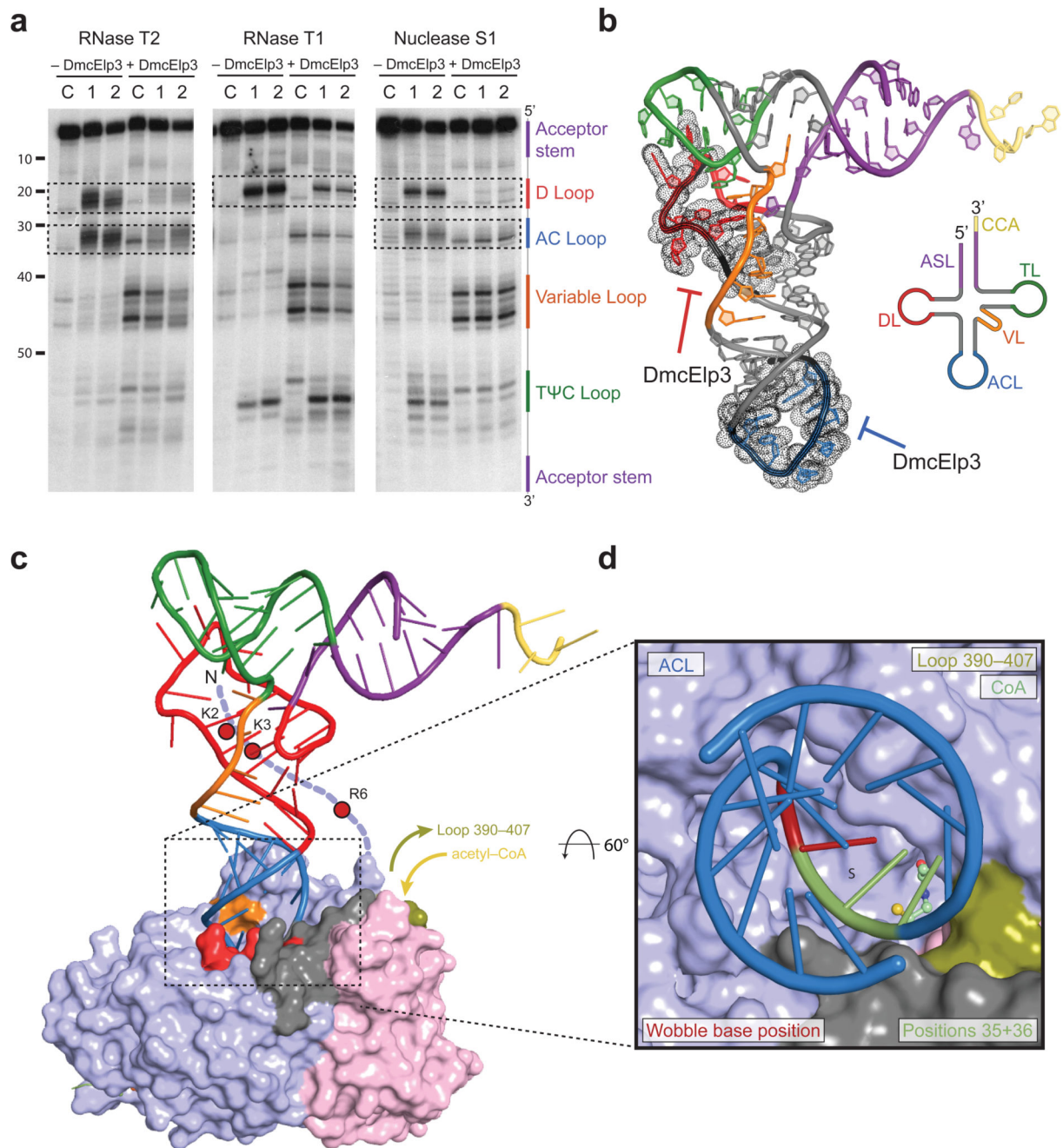
Figure 4. RNase protection assays and tRNA–DmcElp3 model.
(**a**) RNase protection assays using different amounts of RNase T2, T1 and nuclease S1 (C-no nuclease; 1, 2-two different amounts of nuclease) in the absence and presence of DmcElp3. Protected areas are indicated. (**b**) Regions protected by DmcElp3 (dots) are mapped onto the crystal structure of tRNA$_{Glu}$ (PDB ID 1G5956). (**c**) Model of the DmcElp3–tRNA complex using restraints from the mutational analyses and RNase protection assays. (**d**) Close-up of the tRNA binding cavity showing the position of the wobble base position (red), the anticodon (green) and bound CoA (balls and sticks).
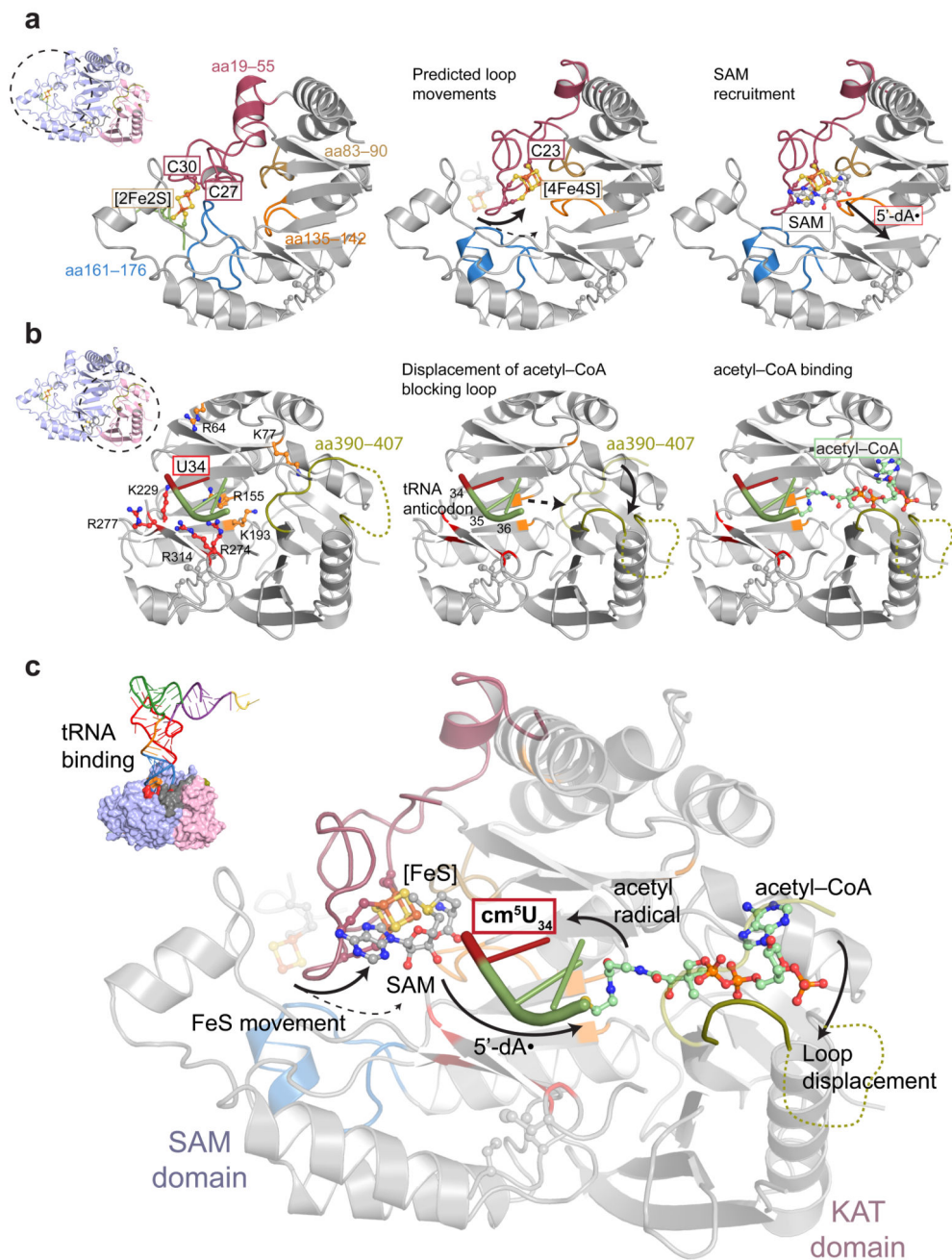
Figure 5. Model of the individual steps of the Elp3 modification reaction.
(**a**) Close-up view on the region of iron-sulfur cluster in the crystal structure of DmcElp3 (left), a model based on the SAM domain structure of RlmN (middle) and the SAM bound state (3RFA; right). Loops that have to undergo movements (arrows) are indicated and labelled (red, blue, brown, orange). (**b**) Close-up view on the tRNA binding region of DmcElp3 in the full length (left) and the 390-407$_{GSGSG}$ structure (middle) with the fitted anticodon from Fig. 4. Localization of the docked acetyl-CoA molecule (right). Single point mutants that affect tRNA binding are indicated in red and orange. (**c**) Summary of the

individual steps of the modification reaction, combining structural data and biochemical data from Huang and colleagues10.

Table 1

Data collection, phasing and refinement statistics

	DmcElp3 Full length SeMet	DmcElp3 390-407$_{GSGSG}$	Fe edge	Zn edge
	PDB ID 5L7J	PDB ID 5L7L		
Data collection				
Space group	C222$_1$	C222$_1$	C222$_1$	C222$_1$
Cell dimensions				
a, b, c (Å)	75.46 158.58 93.58	73.76 161.41 93.22	75.26 160.22 93.65	75.28 159.81 93.43
$\alpha\ \beta\ \gamma$ (°)	90, 90, 90	90, 90, 90	90, 90, 90	90, 90, 90
Wavelength	0.97923	1.0332	1.7377	1.28238
Resolution (Å) [†]	50-2.15(2.2-2.15)	50.0-2.6 (2.66-2.6)	50-2.7 (2.76-2.69)	50-2.9 (2.96-2.89)
R_{meas}	8.3 (230.9)	12.6 (297.4)	11.8 (171.8)	9.3 (203.6)
$I/\sigma(I)$	14.17 (1.03)	14.82 (0.94)	16.43 (1.34)	13.00 (1.00)
$CC_{1/2}$	0.99 (0.56)	0.99 (0.37)	0.99 (0.47)	0.99 (0.42)
Completeness (%)	99.5 (96.8)	99.6 (94.9)	99.4 (92.7)	99.2 (89.8)
Redundancy	10.9 (10.6)	13.0 (11.8)	13.1 (10.4)	6.9 (5.8)
Refinement				
Resolution (Å)	50-2.15	50-2.6		
No. reflections	58703	17582		
R_{work} / R_{free}	19.1/21.9	18.2/21.9		
No. atoms				
Protein	3442	3081		
Ligand/ion (FeS, Zn)	5	5		
Water	38	0		
B factors				
Protein	80.8	90.9		
Ligand/ion	79.0	89.2		
Water	62.7	0		
r.m.s deviations				
Bond lengths (Å)	0.002	0.004		
Bond angles (°)	0.621	0.684		

[a]Values in parentheses are for highest-resolution shell.

[†]Resolution limits according to I/σ of 2 are 2.3 Å for DmcElp3 full length and 2.8 Å for DmcElp3 390-407$_{GSGSG}$